Atmos. Meas. Tech., 17, 4687–4694, 2024
https://doi.org/10.5194/amt-17-4687-2024

Atmospheric Measurement Techniques
Open Access
EGU

On the temperature stability requirements of free-running Nd:YAG lasers for atmospheric temperature profiling through the rotational Raman technique

José Alex Zenteno-Hernández[1,2], Adolfo Comerón[2], Federico Dios[2], Alejandro Rodríguez-Gómez[2], Constantino Muñoz-Porcar[2], Michaël Sicard[2,3], Noemi Franco[4], Andreas Behrendt[5], and Paolo Di Girolamo[4]

[1]Instituto Nacional de Astrofísica, Óptica y Electrónica (INAOE), 72840 Puebla, Mexico
[2]CommSensLab, Dept. of Signal Theory and Communications, Universitat Politècnica de Catalunya (UPC), 08034 Barcelona, Spain
[3]Laboratoire de l'Atmosphère et des Cyclones (LACy), Université de la Réunion, Saint Denis, 97744, France
[4]Scuola di Ingegneria, Università della Basilicata, 85100 Potenza, Italy
[5]University of Hohenheim, Institute of Physics and Meteorology, 70599 Stuttgart, Germany

Correspondence: Adolfo Comerón (comeron@tsc.upc.edu)

Received: 29 February 2024 – Discussion started: 11 March 2024
Revised: 30 May 2024 – Accepted: 17 June 2024 – Published: 13 August 2024

Abstract. We assess the temperature stability requirements of unseeded Nd:YAG lasers in lidar systems for atmospheric temperature profiling through the rotational Raman technique. Taking as a reference a system using a seeded laser assumed to emit pulses of negligible spectral width and free of wavelength drifts, we estimate first the effect of the pulse spectral widening of the unseeded laser on the output of the interference filters, and then we derive the limits of the allowable wavelength drift for a given bias in the temperature measurement that would add to the noise-induced uncertainty. Finally, using spectroscopic data, we relate the allowable wavelength drift to allowable temperature variations in the YAG rod. We find that, in order to keep the bias affecting atmospheric temperature measurements smaller than 1 K, the Nd:YAG rod temperature should also be kept within a variation range of 1 K.

1 Introduction

Profiles of humidity and temperature throughout the troposphere are of the utmost importance for weather forecasting (WMO, 2020). Radiosondes are the staple way to provide such profiles; nevertheless, out of specific measurement campaigns, radiosondes are launched only every 12 h from most meteorological-service sites; on the other hand, Raman lidars can operate on a 24/7 basis, obtaining time resolutions in the range from minutes to a few hours. Therefore, Raman lidars offer an alternative to retrieve these profiles with relatively high temporal resolution without expending balloons and their payloads. With respect to temperature profiles, the Raman lidar technique is based on the dependence on temperature of the intensity of the atmospheric N_2 and O_2 rotational Raman lines (Cooney, 1972). In the typically observed range of atmospheric temperatures, the backscatter cross section corresponding to the Raman lines with low rotational quantum numbers tends to decrease when the temperature increases, while that corresponding to lines with high rotational quantum numbers has the opposite behavior. Therefore, the power ratio of the backscattered radiation in these two spectral regions provides information on the temperature of the backscattering volume.

In the past, the separation of the backscatter of different regions of the pure rotational Raman spectrum has been implemented through the use of diffraction gratings and spatial filtering (Arshinov et al., 1983), and some current systems use a similar technique directing the radiation of different rotational Raman lines to the ends of different optical fibers (Martucci et al., 2021). The current state of the art permits

the use of interference filters to do that separation (Vaughan et al., 1993; Behrendt and Reichardt, 2000).

The power ratio of the filter outputs corresponding to the different regions of the spectrum needs to be calibrated to retrieve the atmospheric temperature. This is usually done by comparison with a radiosonde profile, e.g., Hammann et al. (2015), although in situ calibrations using local light sources (Vaughan et al., 1993) or by constructing a model of the power ratio between the outputs of the filters for high and low quantum numbers (Mahagammulla Gamage et al., 2019) are also described in the literature. For the calibration to be valid over long periods, the stability of the system to ensure that the filters' response keeps constant in time is of paramount importance. Modern interference filters can have temperature dependences between 2 and 5 pm $°C^{-1}$ (Johansen et al., 2017) and, being usually kept in a controlled environment where temperature can be easily stabilized, their response stability is usually not an issue. Of more concern regarding system stability is the laser wavelength. Although some systems use free-running lasers (Di Girolamo et al., 2004; Mahagammulla Gamage et al., 2019), laser frequency stability is achieved in many systems through the use of injection-seeded lasers, where the stability and spectral purity of the seeder is transferred to the host laser (Behrendt and Reichardt, 2000; Behrendt et al., 2002, 2004; Lange et al., 2019), which is forced to operate in a single longitudinal mode. As the cost of a free-running laser is much lower than that of a seeded laser for equivalent output energies, the use of the former can be of advantage, provided the cost of achieving the wavelength stability assessed in the present paper does not offset the reduction in laser cost.

In this paper we assume that the receiver is in a well-controlled environment such that the wavelength drift of the filters can be neglected. We focus henceforth on the wavelength stability requirements for a Nd:YAG non-seeded laser to be used in a lidar measuring atmospheric temperature profiles using the pure rotational Raman spectra of N_2 and O_2 under the excitation by the third harmonic of the laser fundamental frequency. In Sect. 2, the short-term spectral widening of a free-running frequency tripled Nd:YAG laser is taken into account. Section 3 considers the far more important effect of temperature variations in the YAG rod. Section 4 presents the conclusions of this work.

2 Effect of short-term emission spectral widening

We assume that a free-running Nd:YAG laser oscillates in the most intense line, i.e., the R2 → Y3 line (Kushida, 1969) at 1064 nm. This line has a gain full width at half maximum of approximately 5 cm^{-1} (Verdeyen, 1989; Sato and Taira, 2012). As only the modes closest to the maximum gain can oscillate, the emission linewidth is considerably narrower. We will assume a typical emission linewidth of the free-running laser of 1 cm^{-1} at 1064 nm (in fact, references Armandillo et al., 1997, and Lumibird, 2020, give a somewhat lower value of approximately 0.7 cm^{-1}), which would result in 3 cm^{-1} at the third-harmonic wavelength. Although this linewidth is made of many competing modes, we will assume that its average over a sufficient number of pulses can be modeled by a Gaussian curve (Armandillo et al., 1997). Under the excitation of a widened emission, the Raman backscatter spectrum lines are widened accordingly; therefore we will consider that each line of backscatter differential cross section σ_i will show a profile as a function of frequency given by

$$f_{\sigma_i}(\nu) = \frac{2\sqrt{\ln 2}\sigma_i}{\sqrt{\pi}\,\Delta\nu} \exp\left[-\frac{4\ln 2\,(\nu-\nu_{0i})^2}{(\Delta\nu)^2}\right], \quad (1)$$

with ν_{0i} the central emission-line frequency and $\Delta\nu$ the full width at half maximum of the excitation spectrum.

For the purpose of comparison, we will consider the filter responses like those in Hammann et al. (2015). These filters were specified after a thorough analysis of the system trade-off between sensitivity to temperature difference and statistical-noise-induced uncertainty (Radlach et al., 2008; Hammann et al., 2015); for this reason, we expect their characteristics (bandwidth and central-wavelength distance to the laser emission line) to be representative of modern Raman temperature lidars using interference filters. Figure 1 shows the widened Cabannes lines and pure rotational Raman backscatter spectrum (in terms of spectral density) of N_2 and O_2 at sea level (NOAA et al., 1976) with the filters of Hammann et al. (2015) and assuming a central wavelength of the excitation radiation of 354.7133 nm, the third-harmonic wavelength of a Nd:YAG laser at a rod temperature of 38 °C (see Sect. 3). Table 1 shows the wavelengths (in vacuum) and wavenumbers considered. The calculation is based on the spectrum frequencies and intensities used in Zenteno-Hernández et al. (2021), which in turn rely on expressions and spectroscopic data found in Murphy et al. (1969), Alms et al. (2008), Buldakov et al. (1996), and Long (2002).

The power at the filter outputs is shown in Fig. 2, under the assumption of a widened spectrum and of an ideal line spectrum. The effect of the Gaussian spectral widening is so small that the pairs of curves are almost undistinguishable. Likewise, the spectral widening effect is very small in the curves (Fig. 3) obtained as the power ratio between the high-quantum-number filter outputs (IF2 and IF3 filters in Fig. 1) and the low-quantum-number filter output (IF1 filter in Fig. 1), henceforth called Q-curves, which, after calibration, give the atmospheric temperature. We conclude that the spectral widening of a free-running laser emission with respect to that of a seeded laser does not have a significant impact on the system performance under the assumption of a Gaussian widening smaller than 1 cm^{-1} at the fundamental wavelength (Armandillo et al., 1997). No leakage of the Cabannes lines into the filters (especially into the low-quantum-number one) would be noticed in these conditions in spite

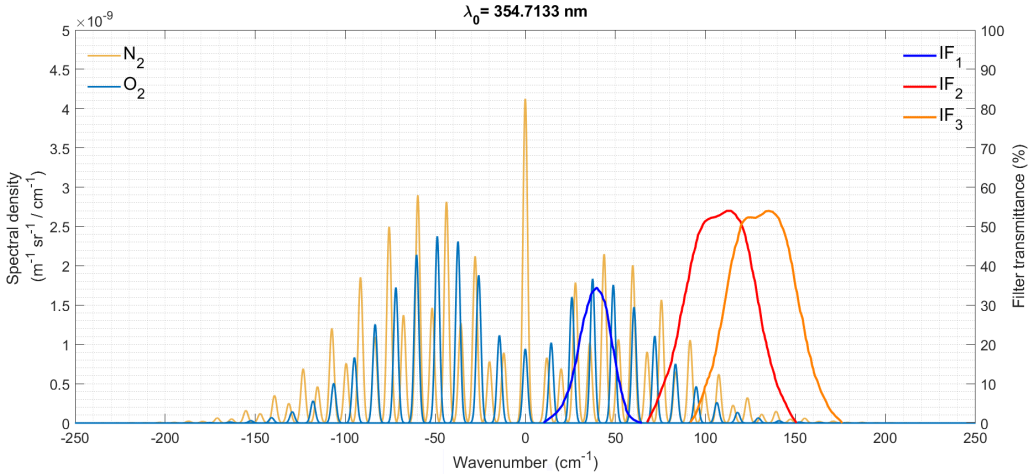

Figure 1. Cabannes lines and pure rotational backscatter Raman spectrum of N_2 (yellow lines) and O_2 (turquoise lines) at sea level under the assumption of a Gaussian-widened excitation at 354.7133 nm. The spectrum is given as the wavenumber shift from the excitation wavenumber. The transmission curves of the filters and combination of filters in Hammann et al. (2015) are superimposed, transposing the wavelength scale in that reference to the wavenumber scale here. The filter denoted as IF2 (red transmission curve) is used in high-background-radiation situations, whereas the IF3 filter (orange line) is optimized for low-background ones. The Cabannes-line amplitudes (zero shift) are divided by 500 to fit them into the graph.

Table 1. Wavelengths and wavenumbers of lasers and filter passbands at half maximum (HM) considered.

	Wavelength (nm)	Wavenumber (cm^{-1})		
Third harmonic of Nd:YAG laser fundamental wavelength	354.7133	28191.78		
	Non-shifted filters		Shifted filters*	
	HM wavelengths (nm)	HM wavenumbers (cm^{-1})	HM wavelengths (nm)	HM wavenumbers (cm^{-1})
Low-quantum-number filter IF1	354.0926–354.3488	28220.78–28241.20	353.9852–354.2412	28229.35–28249.77
High-quantum-number filter IF2	353.0767–353.6324	28277.95–28322.46	352.9699–353.5253	28286.52–28331.03
High-quantum-number filter IF3	352.7945–353.3415	28301.23–28345.11	352.7945–353.3415	28309.80–28353.68

* See Sect. 3. A shift of 8.57 cm^{-1} is considered in the filter passbands with respect to those non-shifted.

of their higher cross section (around 2 orders of magnitude) with respect to the next more intense lines of the rotational Raman spectrum. One should make sure that this hypothesis is satisfied in particular cases and that the presence of aerosols does not increase the return at the excitation wavelength so as to produce leakage.

3 Effect of central wavelength drift

We now turn to the effect of drift of the laser central wavelength. In an unseeded Nd:YAG laser, the central wavelength coincides with the center of the gain curve, which in turn depends on the rod temperature. We have used the approximate analytical models in Sato and Taira (2012) that reproduce very well experimental results of the central frequency temperature dependence of various Nd:YAG emission lines, among which is the one corresponding to the R2 → Y3 transition, in the temperature range 15–350 °C. For the benefit of the reader, we reproduce here Eq. (6) of Sato and Taira (2012):

$$\nu_{\mathrm{if}}(T) = \nu_{\mathrm{if}}(0) - c_{\mathrm{if}}\left(\frac{T}{\Theta_{\mathrm{D}}}\right)^4 \int_0^{\frac{\Theta_{\mathrm{D}}}{T}} \frac{x^3}{e^x - 1}\mathrm{d}x, \quad (2)$$

where ν_{if} is the central wavenumber, T is the temperature, Θ_{D} is the Debye temperature, and c_{if} is a fitting parameter. In

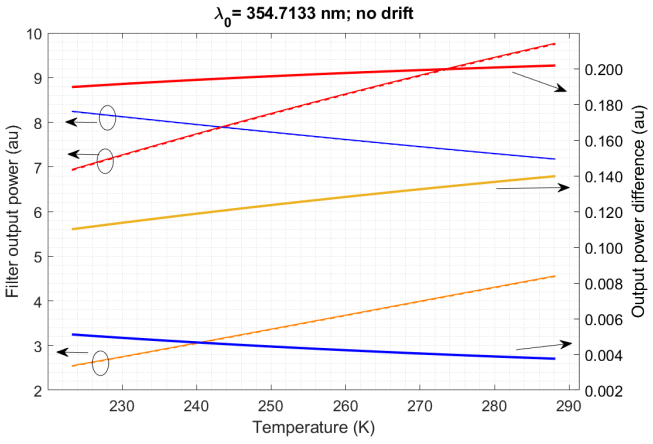

Figure 2. Left vertical axis: power (in arbitrary units) at the filter outputs for the widened spectrum (dashed curve) and for an unwidened spectrum (continuous curve) as a function of the atmospheric temperature. The colors of the curves indicate the corresponding filter according to the colors of transmission curves in Fig. 1. There are two curves for each color, but the effect of the Gaussian widening of the spectrum lines is so small that they are almost undistinguishable. Right vertical axis: differences in the filter output power between the unwidened and the widened spectrum. The scale is in the same arbitrary units as the left vertical scale. The colors of the curves indicate the corresponding filter according to the colors of transmission curves in Fig. 1.

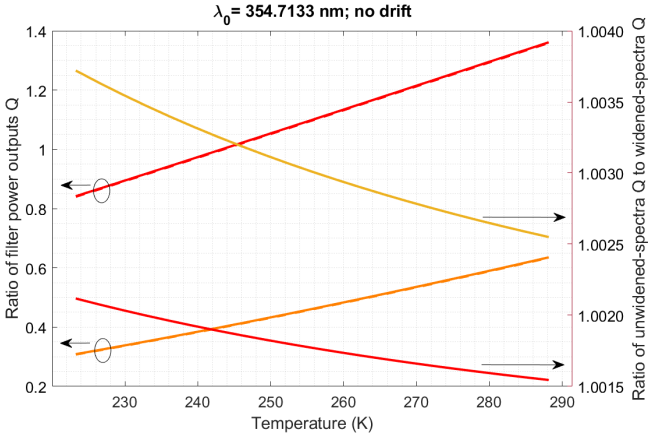

Figure 3. Left vertical axis: ratio (Q) between the outputs of the IF2 filter (red) and the IF1 filter (blue) of Fig. 1 (red lines) and between the outputs of the IF3 filter (orange) and the IF1 filter (orange lines) as a function of the atmospheric temperature. The lines corresponding to the widened spectrum (dashed) and those corresponding to the unwidened spectrum (continuous) are almost undistinguishable. Right vertical axis: ratios of the Q obtained with unwidened spectrum to the Q obtained with widened spectrum. The red curve corresponds to the ratio of Qs between the IF2 filter and the IF1 filter and the orange line to the ratio of Qs between the IF3 filter and the IF1 filter.

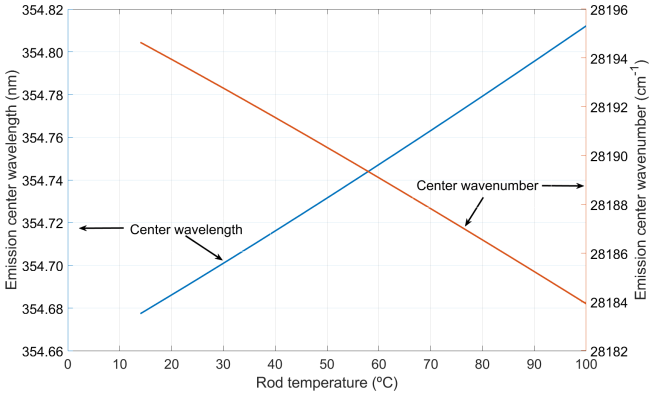

Figure 4. Dependence of the third-harmonic emission center wavelength and center wavenumber on the rod temperature.

particular we have taken the transition wavenumber at 0 K as 9403.15 cm^{-1}, the fitting parameter for temperature dependence c_{if} as 130.6 cm^{-1} and the Debye temperature as 795 K (Sato and Taira, 2012) (see also Table 1 of this reference). Figure 4 shows the dependence of the center of the third-harmonic wavelength emission with the temperature according to that model. The dependence is nearly linear with a slope of approximately 1.5 pm °C^{-1}.

To assess the variations in the Q-curve with the laser central wavelength, we assume the central wavelength of 354.7133 nm and the widened spectrum of the unseeded laser already considered in the previous section, and we let it drift by ±1.5 pm, which would correspond to a temperature variation in the Nd:YAG rod of slightly less than ±1 around 38 °C. The effect of the wavelength drift on the power at the filter outputs is shown in Fig. 5, where small differences can be seen (more noticeable in the IF2 (red) filter output). However small, these differences impact the Q-curves, as shown in Fig. 6, and imply an uncertainty in the temperature retrieval. For example, let us consider Fig. 7, which is a zoom of the right-hand panel of Fig. 6 around the temperature of 260 K (with the horizontal and vertical axes swapped), where we assume that the Q-curve has been calibrated for a laser rod temperature at 38 °C (solid curve). If the laser central wavelength drifts subsequently by ±1.5 pm, roughly corresponding to a temperature variation in the laser rod of ±1 °C, the uncertainty in the retrieved temperature for the approximate 0.4835 value of Q is the atmospheric temperature interval encompassed by the double-arrowed line, i.e., slightly more than 1 K.

This assessment has been done for the laser central wavelength of 354.7133 nm and a drift of ±1.5 pm around it. However, in Hammann et al. (2015), the laser wavelength was 354.83 nm, fixed by the seeder wavelength. If we assume that the filter responses in Fig. 1 can be shifted by 116.7 pm (i.e., around 9 cm^{-1}) towards shorter wavelengths while preserving their shape in order to be in a similar filter passband situation with respect to the Raman spectrum as in

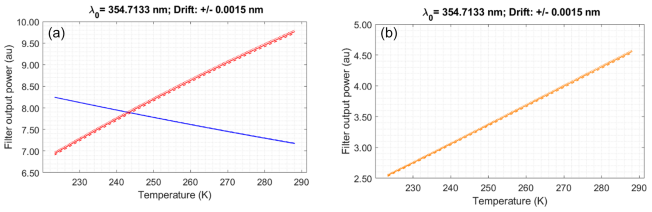

Figure 5. Effect of the wavelength drift on the power (in relative units) at the filter outputs. **(a)** IF1 (blue) and IF2 (red) filters of Fig. 1. **(b)** IF3 (orange) filter of Fig. 1. Solid lines correspond to the filter outputs at the 354.7133 nm wavelength. The dashed line corresponds to the +1.5 pm drift and the dotted one to the −1.5 pm one. Note that the spans of the vertical axis scale in the left and right panels are not the same.

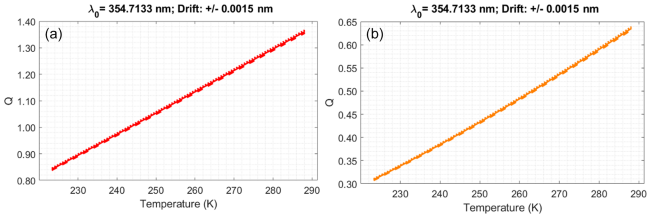

Figure 6. Effect of the wavelength drift on the Q ratio. **(a)** Ratio between the output power of the IF2 (red) filter and the IF1 (blue) filter of Fig. 1. **(b)** Ratio between the output power of the IF3 (orange) filter and the IF1 (blue) filter of Fig. 1. Solid lines correspond to the filter outputs at the 354.7133 nm wavelength. The dashed line corresponds to the +1.5 pm drift and the dotted one to the −1.5 pm one. Note that the spans of the vertical axis scale in the left and right panels are not the same.

Hammann et al. (2015), we obtain, for the ratio of IF3 (orange) filter output power to the IF1 (blue) filter output power, the curves of Fig. 8, where the uncertainty in the retrieval of the temperature around 260 K, because of a non-controlled ±1.5 pm laser wavelength drift from the calibration wavelength, is slightly smaller than 1 K. Note that we have implicitly assumed trailing zeros in the wavelength of the laser in Hammann et al. (2015), which is given only to the hundredth of nanometers; what is important however is that by shifting the filters by around 9 cm^{-1} we operate in a region where the sensitivity of the Q-curve to wavelength drifts is smaller.

The uncertainty in the temperature retrieval due to a ±1.5 pm wavelength drift with respect to the calibration wavelength has been estimated as in the examples above illustrated in Figs. 7 and 8 for the entire considered temperature range and is shown in Fig. 9 for the case of the filters shifted by 8.57 cm^{-1}. The uncertainty varies between approximately 0.87 K at a temperature of 220 K and 1.22 K at 290 K, considering that the calibrated Q-curve has been obtained as the ratio of the output power of the IF2 filter of Fig. 1 to the output power of the IF1 filter. For the Q-curve given by the ratio of the output power of the IF3 filter of

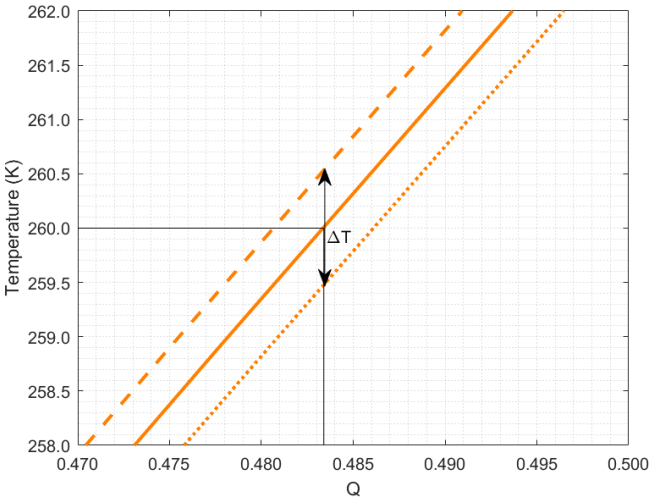

Figure 7. Example of uncertainty in the temperature retrieval (ΔT) due to the uncertainty in the laser central wavelength. Solid curve: assumed calibrated Q obtained as the ratio between the output powers of the IF3 (orange) filter and the IF1 (blue) filter of Fig. 1 at the 354.7133 nm wavelength. Dashed and dotted curves: Q obtained for wavelength deviations with respect to the calibration wavelengths of +1.5 and −1.5 pm respectively. Note that the axes are swapped with respect to those in Fig. 6 to emphasize that Q is the variable from which the temperature is retrieved.

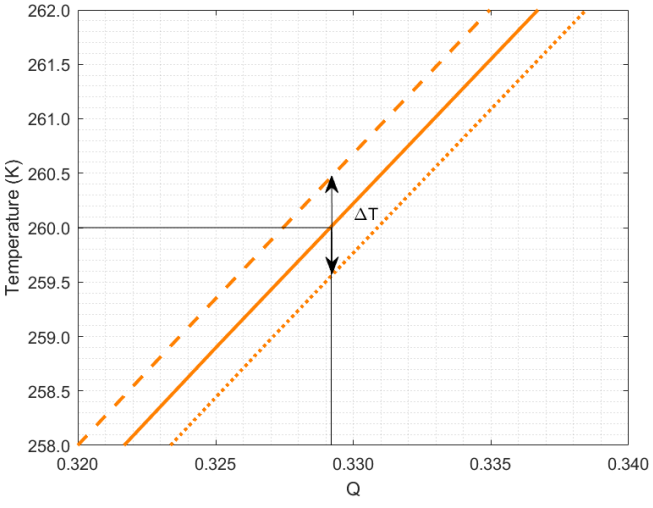

Figure 8. Like Fig. 7 with the filters of Fig. 2 shifted 8.57 cm^{-1} towards shorter wavelengths.

Fig. 1 and the IF1 filter, the uncertainty ranges between 0.77 at 220 K and 1.07 at 290 K.

4 Conclusions

We have estimated, using a real filter configuration, that in lidar systems employing a Nd:YAG laser to measure the atmospheric temperature profiles through the pure rotational

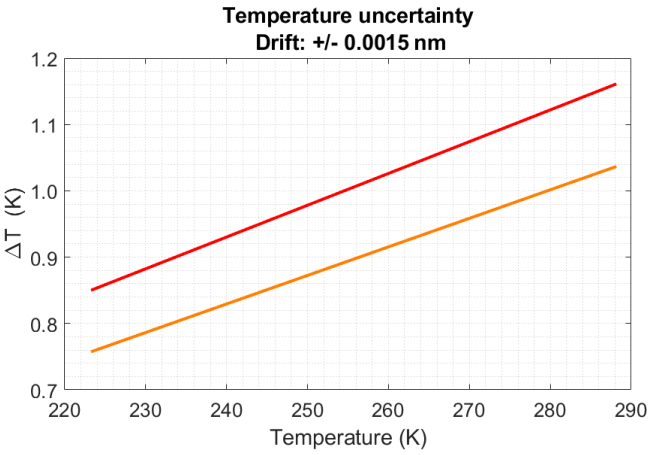

Figure 9. Retrieved atmospheric temperature uncertainty due to a ± 1.5 pm wavelength drift over the entire considered temperature range for Q obtained as the ratio between the output powers of the IF2 (red) filter and the IF1 (blue) filter of Fig. 1 (red curve) and as the ratio between the outputs of the IF3 (orange) filter and the IF1 (blue) filter in the same figure (orange curve). The filter responses have been shifted by $8.57\,\mathrm{cm}^{-1}$.

Raman technique, the short-term spectral widening of a commercial-grade unseeded laser virtually does not affect the ratio of the output power of the high-quantum-number filter to the output power of the low-quantum-number filter (Q-curves), at least under the assumption that the widening is Gaussian (Armandillo et al., 1997) with a full width at half maximum smaller than $1\,\mathrm{cm}^{-1}$ at the fundamental wavelength. One should pay attention that aerosols do not increase the elastic return to the point that leakage into the filters can happen. For example, the ratio between the peaks of the Cabannes lines and the peak of the closest O_2 line in the anti-Stokes rotational Raman spectrum is about 2000; on the other hand, the backscatter coefficient of dense clouds at 355 nm can typically be up to 500 times the molecular backscatter coefficient at that wavelength; hence a suppression sufficiently higher than 10^6 (optical density 6) should be achieved at the emission wavelength by the filter to keep the effect of clouds negligible. A suppression of 10^6 would be sufficient for most aerosol scenarios. However, slight drifts on the central wavelength of the laser emission spectrum entail small changes in the Q-curves that impair the calibration and cause an uncertainty in the retrieved atmospheric temperature. The drifts can be related to temperature changes in the YAG rod. For the third harmonic of the laser, the drift is around $1.5\,\mathrm{pm}\,^{\circ}\mathrm{C}^{-1}$. The allowable uncertainty in the temperature retrieval depends of course on the application, but if we take as a reference value ± 1 K, it turns out that the YAG rod temperature also needs to be kept within ± 1 K. Note en passant that, in a seeded laser, changes in temperature in the seeder could also cause wavelength drifts, consequently uncontrolled biases in the atmospheric temperature measurements that would add to their uncertainty.

Note that, knowing the temperature coefficients of the filters, the analysis could be readily extended to their temperature stability requirements, but this is not the focus of the present study. Likewise, a similar analysis could be carried out for a system working at 532 nm if the filter specifications were known. We have limited the study to an ultraviolet system because the $1/\lambda^4$ law of the Raman cross section and the lesser background radiation give it an advantage over the visible one, even if the transmitted energy per pulse is lower.

It must be stressed that the analysis above takes only into account the temperature uncertainty due to the spectral behavior of the laser radiation. Although out of the scope of this work, it can be noted that, taking as reference the temperature drifts of the filters quoted in Johansen et al. (2017), the thermal management of the filter enclosure should be stricter than that of the laser rod. However, as the latter has to cope with heat generated by the pumping system, it is considered more critical. To this, the uncertainty due to the limited signal-to-noise ratio in the detected power should be added (Behrendt and Reichardt, 2000; Di Girolamo et al., 2004).

Code availability. A code to reproduce the results of this article can be easily written from the spectroscopic data found in Murphy et al. (1969, https://doi.org/10.1366/000370269774380824), Alms et al. (2008, https://doi.org/10.1063/1.431821), Buldakov et al. (1996, https://doi.org/10.1016/0584-8539(95)01631-7), and Long (2002, https://doi.org/10.1002/0470845767), conveniently summarized in Appendix A of Zenteno-Hernández et al. (2021, https://doi.org/10.3390/S21041277). The code writer must substitute the spectral lines at wavenumber ν_{0i}, generated by those data, for functions of the form given by Eq. (1).

Data availability. No data sets were used in this article.

Author contributions. JAZ: formal analysis, software. AC: conceptualization, writing. FD: methodology, formal analysis. AR: visualization, supervision. CM: software, visualization. MS: visualization. NF: validation. AB: supervision, visualization. PDG: supervision, review, editing.

Competing interests. The contact author has declared that none of the authors has any competing interests.

Disclaimer. Publisher's note: Copernicus Publications remains neutral with regard to jurisdictional claims made in the text, published maps, institutional affiliations, or any other geographical representation in this paper. While Copernicus Publications makes every effort to include appropriate place names, the final responsibility lies with the authors.

Acknowledgements. Author José Alex Zenteno-Hernández thanks CONACyT for the 2018-000068-02NACF-29418 scholarship. The authors with Universitat Politècnica de Catalunya wish to acknowledge the support of Spain's State Agency for Research (AEI), of the Catalan Regional Government, and of the European Commission's Directorate-General for Research and Innovation through the EU Horizon 2020 and Horizon Europe programs. The contribution of Paolo Di Girolamo and Noemi Franco to this paper was possible thanks to the support from the Italian Ministry for Education, University and Research; the support of the Italian Space Agency; and the support of the European Commission through the European Regional Development Fund.

Financial support. This research has been supported by the Consejo Nacional de Ciencia y Tecnología (grant no. 2018-000068-02NACF-29418); the Agencia Estatal de Investigación (project RESA-CI, grant no. PID2019-103886RB-I00); the Agència de Gestió d'Ajuts Universitaris i de Recerca (grant no. 2021 SGR 01415); EU Horizon 2020 (project ACTRIS IMP, grant no. 871115, and project ATMO-ACCESS, grant no. 101008004); Horizon Europe (project REALISTIC, grant no. 101086690); the Ministero dell'Istruzione, dell'Università e della Ricerca (grants OT4CLIMA and FISR2019-CONCERNING); the Agenzia Spaziale Italiana (grants As-ATLAS and CALIGOLA); and the European Regional Development Fund, European Observation Network for Territorial Development and Cohesion (grant no. FESR 2014-2022 "STAC-UP").

Review statement. This paper was edited by Robin Wing and reviewed by two anonymous referees.

References

Alms, G. R., Burnham, A. K., and Flygare, W. H.: Measurement of the dispersion in polarizability anisotropies, J. Chem. Phys., 63, 3321, https://doi.org/10.1063/1.431821, 2008.

Armandillo, E., Norrie, C., Cosentino, A., Laporta, P., Wazen, P., and Maine, P.: Diode-pumped high-efficiency high-brightness Q-switched ND:YAG slab laser, Opt. Lett., 22, 1168, https://doi.org/10.1364/ol.22.001168, 1997.

Arshinov, Yu. F., Bobrovnikov, S. M., Zuev, V. E., and Mitev, V. M.: Atmospheric temperature measurement using a pure rotational Raman lidar: comment, Appl. Optics, 22, 2984–2990, https://doi.org/10.1364/ao.22.002984, 1983.

Behrendt, A. and Reichardt, J.: Atmospheric temperature profiling in the presence of clouds with a pure rotational Raman lidar by use of an interference-filter-based polychromator, Appl. Optics, 39, 1372, https://doi.org/10.1364/ao.39.001372, 2000.

Behrendt, A., Nakamura, T., Onishi, M., Baumgart, R., and Tsuda, T.: Combined Raman lidar for the measurement of atmospheric temperature, water vapor, particle extinction coefficient, and particle backscatter coefficient, Appl. Optics, 41, 7657, https://doi.org/10.1364/ao.41.007657, 2002.

Behrendt, A., Nakamura, T., and Tsuda, T.: Combined temperature lidar for measurements in the troposphere, stratosphere, and mesosphere, Appl. Optics, 43, 2930–2939, https://doi.org/10.1364/AO.43.002930, 2004.

Buldakov, M. A., Ippolitov, I. I., Korolev, B. V., Matrosov, I. I., Cheglokov, A. E., Cherepanov, V. N., Makushkin, Y. S., and Ulenikov, O. N.: Vibration rotation Raman spectroscopy of gas media, Spectrochim. Acta A Mol. Biomol. Spectrosc., 52, 995–1007, https://doi.org/10.1016/0584-8539(95)01631-7, 1996.

Cooney, J.: Measurement of Atmospheric Temperature Profiles by Raman Backscatter, J. Appl. Meteorol. Clim., 11, 108–112, https://doi.org/10.1175/1520-0450(1972)011<0108:MOATPB>2.0.CO;2, 1972.

Di Girolamo, P., Marchese, R., Whiteman, D. N., and Demoz, B. B.: Rotational Raman Lidar measurements of atmospheric temperature in the UV, Geophys. Res. Lett., 31, 1–5, https://doi.org/10.1029/2003GL018342, 2004.

Hammann, E., Behrendt, A., Le Mounier, F., and Wulfmeyer, V.: Temperature profiling of the atmospheric boundary layer with rotational Raman lidar during the HD(CP)^2 Observational Prototype Experiment, Atmos. Chem. Phys., 15, 2867–2881, https://doi.org/10.5194/acp-15-2867-2015, 2015.

Johansen, A., Czajkowski, A., Scobey, M., Egerton, P., and Fortenberry, R.: Thin-film interference filters for LIDAR, ALLUXA White Paper, 13 pp., https://alluxa.com/wp-content/uploads/2017/04/Alluxa-Thin-Film-Interference-Filters-for-LIDAR.pdf (last access: 26 July 2024), 2017.

Kushida, T.: Linewidths and thermal shifts of spectral lines in neodymium-doped yttrium aluminum garnet and calcium fluorophosphate, Phys. Rev., 185, 500–508, https://doi.org/10.1103/PhysRev.185.500, 1969.

Lange, D., Behrendt, A., and Wulfmeyer, V.: Compact Operational Tropospheric Water Vapor and Temperature Raman Lidar with Turbulence Resolution, Geophys. Res. Lett., 46, 14844–14853, https://doi.org/10.1029/2019GL085774, 2019.

Long, D. A.: The Raman effect: a unified treatment of the theory of Raman scattering by molecules, John Wiley & Sons Ltd, Hoboken, NJ, USA, 21–22, https://doi.org/10.1002/0470845767, 2002.

Lumibird: Q-smart 450 & 850, Compact pulsed Nd:YAG lasers brochure, 2 pp., http://www.lumibird.cn/uploads/file/20201218/20201218113604_67241.pdf (last access: 26 July 2024), 2020.

Mahagammulla Gamage, S., Sica, R. J., Martucci, G., and Haefele, A.: Retrieval of temperature from a multiple channel pure rotational Raman backscatter lidar using an optimal estimation method, Atmos. Meas. Tech., 12, 5801–5816, https://doi.org/10.5194/amt-12-5801-2019, 2019.

Martucci, G., Navas-Guzmán, F., Renaud, L., Romanens, G., Gamage, S. M., Hervo, M., Jeannet, P., and Haefele, A.: Validation of pure rotational Raman temperature data from the Raman Lidar for Meteorological Observations (RALMO) at Payerne, Atmos. Meas. Tech., 14, 1333–1353, https://doi.org/10.5194/amt-14-1333-2021, 2021.

Murphy, W. F., Holzer, W., and Bernstein, H. J.: Gas Phase Raman Intensities: A Review of "Pre-Laser" Data, Appl. Spectrosc., 23, 211–218, https://doi.org/10.1366/000370269774380824, 1969.

NOAA, NASA, and USAF: U.S. Standard Atmosphere, NOAA–S/T 76–1562, 243 pp., https://www.ngdc.noaa.gov/stp/space-weather/online-publications/miscellaneous/us-standard-atmosphere-1976/us-standard-atmosphere_st76-1562_noaa.pdf (last access: 26 July 2024), 1976.

Radlach, M., Behrendt, A., and Wulfmeyer, V.: Scanning rotational Raman lidar at 355 nm for the measurement of tropospheric temperature fields, Atmos. Chem. Phys., 8, 159–169, https://doi.org/10.5194/acp-8-159-2008, 2008.

Sato, Y. and Taira, T.: Temperature dependencies of stimulated emission cross section for Nd-doped solid-state laser materials, Opt. Mater. Express., 2, 1076, https://doi.org/10.1364/ome.2.001076, 2012.

Vaughan, G., Wareing, D. P., Thomas, L., Pepler, S. J., and Mitev, V.: Atmospheric temperature measurements made by rotational Raman scattering, Appl. Optics, 32, 2758–2764, https://doi.org/10.1364/AO.32.002758, 1993.

Verdeyen, J. T.: Laser electronics, Prentice-Hall, Englewood Cliffs, NJ, USA, ISBN: 013523655X, 1989.

WMO: Statement of Guidance for Global Numerical Weather Forecasting (GNWP), 12 pp., https://wmoomm.sharepoint.com/:b:/s/wmocpdb/ETYXQ5jomShFk7O78PVlJkYBpthX5-FlO04_F3mLqGb3ug?e=QQkD8B (last access: 24 June 2023), 2020.

Zenteno-Hernández, J. A., Comerón, A., Rodríguez-Gómez, A., Muñoz-Porcar, C., D'Amico, G., and Sicard, M.: A comparative analysis of aerosol optical coefficients and their associated errors retrieved from pure-rotational and vibro-rotational raman lidar signals, Sensors (Switzerland), 21, 1–21, https://doi.org/10.3390/S21041277, 2021.